Protocol dependent frictional granular jamming simulations: cyclical, compression and expansion

A. P. Santos[1,*], Ishan Srivastava[2], Leonardo E. Silbert[3], Jeremy B. Lechman[4], and Gary S. Grest[4]

[1]*AMA Inc., Thermal Protection Materials Branch, NASA Ames Research Center, Moffett Field, CA 94035, USA.*

[2]*Center for Computational Sciences and Engineering, Lawrence Berkeley National Laboratory, Berkeley, California 94720, USA.*

[3]*School of Math, Science and Engineering, Central New Mexico Community College, Albuquerque, NM 87106, USA.*

[4]*Sandia National Laboratories, Albuquerque, NM 87185, USA.*

[*]*Correspondance: andrew.p.santos@nasa.gov*

February 3, 2024

Abstract

Granular matter takes many paths to pack in natural and industrial processes. The path influences the packing microstructure, particularly for frictional grains. We perform discrete element modeling simulations of different paths to construct packings of frictional spheres. Specifically, we explore four stress-controlled protocols implementing packing expansions and compressions in various combinations thereof. We characterize the eventual packed states through their dependence of packing fraction and coordination number on packing pressure, identifying non-monotonicities with pressure that correlate with the fraction of frictional contacts. These stress-controlled, bulk-like particle simulations access very low-pressure packings, namely the marginally stable limit, and demonstrate the strong protocol dependence of frictional granular matter.

1 Introduction

Packings of granular materials are relevant to many industrial processes and natural phenomena. Prediction and control of particle packing in industrial processes for particulate materials significantly impacts property repeatability, such as additive manufactured part strength assurance (Snow *et al.*, 2019; Wischeropp *et al.*, 2019). Packings formed by natural forces, from hydrological (Gerhard and Reich, 2000) to astronomical (Watanabe *et al.*, 2019), or animal (Weiner *et al.*, 2020; Buarque de Macedo *et al.*, 2021), rarely follow single, straight-forward protocols, which leads to variable, or in some cases optimized, properties. Understanding the complex response of these far-from-equilibrium granular packings is critical to developing more efficient and effective means of controlling them.

Simulations use access to particle-scale information, such as particle-particle forces, to study the effect of packing protocol in ideal and realistic material. Simulations have shown that frictionless sphere packings approach the maximally random jammed state volume fraction (Torquato *et al.*, 2000) and the coordination number set by isostaticity (O'Hern *et al.*, 2003) for many different packing protocols. However the jamming point depends on material-specific contact mechanics and protocol (Luding, 2016; Santos *et al.*, 2020). Frictionless particle packings can lead to various packing fractions by protocol changes in isotropic compression (Chaudhuri

et al., 2010) or by applying shear strains (Bertrand *et al.*, 2016; Srivastava *et al.*, 2022). Real granular particles have friction, and can form looser packings than frictionless spheres (Onoda and Liniger, 1990; Silbert, 2010; Santos *et al.*, 2020). Frictional particles access a greater range of packing fraction depending on the protocol and the particle friction coefficient. Song *et al.* (2008) attributed the range of packing fractions to sampling an ensemble of jammed states in a statistical mechanical definition of jamming. Friction also modulates the coordination number - the average number of particles each particle is in contact with - Z, which decreases gradually from the frictionless value of $Z = 6$ to the frictional isostatic value of Z=4 as the coefficient of friction increases (Silbert *et al.*, 2002; Shundyak *et al.*, 2007; Somfai *et al.*, 2007; Song *et al.*, 2008; Silbert, 2010; Santos *et al.*, 2020). The coordination number and packing volume fraction ϕ - defined as the ratio of the volume occupied by all the particles to that of the container volume - of stable packings of particles with a specific friction coefficient can depend on the protocol (Silbert *et al.*, 2002; Somfai *et al.*, 2007; Bi *et al.*, 2011).

Bililign *et al.* (2019) observed protocol dependence in experiments of two-dimensional packings under various protocols, for example uni- and bi-axial compression. A common method to create dense particle packings is by isotropic compression. Volume-controlled compression can be achieved by randomly distributing point particles in a simulation cell and increasing the diameter (Lubachevsky and Stillinger, 1990; Shundyak *et al.*, 2007), or by decreasing the simulation cell density of an over-compressed system, while minimizing the conformational energy (O'Hern *et al.*, 2002; Charbonneau *et al.*, 2012). Flowing particles coming to a stop is another way for them to pack, for example from flow down an incline (Silbert *et al.*, 2002) or by applying shear (Bi *et al.*, 2011; Srivastava *et al.*, 2019, 2022). Disrupting or re-packing already packed systems are also common methods to modulate packing fraction, such as tapping or cyclical shear. These repetitive processes generally lead to denser packings (Kohlrausch, 1854; Williams and Watts, 1970; Knight *et al.*, 1995; Philippe and Bideau, 2002; Richard *et al.*, 2005; Rosato *et al.*, 2010; Kumar and Luding, 2016).

Simulation packing methods often control the volume, not the stress. Achieving zero-stress stable packings is difficult for such methods. Previous jamming studies of particles with sliding friction as a function of pressure demonstrated that the packing fraction and the coordination number decrease monotonically with decreasing pressure (Shundyak *et al.*, 2007; Silbert, 2010). In this article, a constant pressure in all directions allows the simulation cell to adjust the edge length, and constant zero shear stresses allow the simulation cell to adopt triclinic configurations. The final packings repeatably and rigorously satisfy those stress conditions. Dagois-Bohy *et al.* (2012); Smith *et al.* (2014) showed that packings formed by controlling the pressure are more stable to shear deformation than volume-controlled methods. Furthermore, very low pressures are accessible to this protocol without extrapolation, unlike previous protocols (Silbert, 2010). Similar protocols have been applied to 2D frictionless (Dagois-Bohy *et al.*, 2012), 3D frictionless (Smith *et al.*, 2014), 2D frictional (Shundyak *et al.*, 2007; Somfai *et al.*, 2007) and 3D frictional (Santos *et al.*, 2020) granular particles.

This work studies how the protocols available to stress-controlled packing simulations change packing properties. Details on the equations of motion for the stress-controlled simulations are in Sec. 2.1. Specifically in this study, a volume-controlled over-compression method is compared to four stress-controlled methods, including over-compression and release, gentle under-compression and cyclical compression and release, and are defined in Sec. 2.2. With zero initial kinetic energy, most of the protocols show similar behavior in Sec. 3.1. A cyclically compressed and expanded packing method has distinct, non-monotonic dependence with respect to the number of cycles and pressure. Sec. 3.2 aims to understand the non-monotonic pressure dependence by analyzing distribution of contact forces. And non-monotonic pressure dependence in the other protocols is investigated by varying protocol parameters like drag and the initial pressure in Sec. 3.2.

2 Methodology

2.1 Constant stress simulations and particle model

Granular particles are modeled as spheres of diameter d and mass m, which only interact when in contact, through a Hookean spring-dashpot-slider interaction potential (Cundall and Strack, 1979). The normal (n) and

tangential (s) particle spring (k) and damping (γ) parameters are set equal to each other $k_n = k_s = 1$ and $\gamma_n = \gamma_s = 0.5\tau^{-1}$ where $\tau = \sqrt{m/k_n}$ is the unit of time. Here, the tangential forces are referred to by the letter 's' to indicate that we include sliding friction between the particles, characterized by the sliding friction coefficient μ_s, as implemented by Cundall and Strack ((Buarque de Macedo *et al.*, 2021), whereby the Coulomb criterion for slipping is satisfied. The unit of pressure is k_n/d and applies to all stresses; the unit of force is $k_n d$. Linear elastic behavior for inter-particle contacts is reasonably accurate as a model for stiff particles at most simulated pressures $P < 10^{-1} k_n/d$. Higher pressures $P \geq 10^{-1} k_n/d$ are simulated to compare with past work, despite large particle overlaps at packing.

Discrete element method (DEM) simulations were performed using LAMMPS (Thompson *et al.*, 2022). The inter-particle forces $\mathbf{F}_i$ and torques $\boldsymbol{\tau}_i$ are used to integrate the equations of motion and update particle positions and orientations. To simulate granular particles under constant stress, the equations of motion include the degrees of freedom for a deforming simulation cell. The granular particles are placed within a periodic three-dimensional simulation cell that maintains an applied stress tensor by allowing triclinic cell deformations. In particular, the Shinoda-Shiga-Mikami (Shinoda *et al.*, 2004) formulation of a barostat was used to integrate the positions and momenta of the particles and to maintain an applied pressure tensor by varying the simulation cell. This formulation combines the hydrostatic equations of Martyna *et al.* with the strain energy proposed by Parrinello and Rahman (Parrinello and Rahman, 1981; Martyna *et al.*, 1994),

$$\dot{\mathbf{r}}_i = \frac{\mathbf{p}_i}{m} + \frac{\mathbf{p}_{\text{cell}}}{\omega_{\text{cell}}}\mathbf{r}_i \tag{1a}$$

$$\dot{\mathbf{p}}_i = \mathbf{F}_i - \frac{\mathbf{p}_{\text{cell}} - \frac{1}{N_f}\text{Tr}[\mathbf{p}_{\text{cell}}]}{\omega_{\text{cell}}}\mathbf{p}_i \tag{1b}$$

$$\dot{\mathbf{h}} = \frac{\mathbf{p}_{\text{cell}}}{\omega_{\text{cell}}}\mathbf{h} \tag{1c}$$

$$\frac{\dot{\mathbf{p}}_{\text{cell}}}{k_{\text{drag}}} = V(\mathbf{P}_{\text{int}} - \mathbf{P}_{\mathbf{a}}) - \mathbf{h}\Sigma\mathbf{h}^T + \frac{1}{N_f}\sum_{i=1}^{N}\frac{\mathbf{p}_i^2}{m}\mathbf{I} \tag{1d}$$

$$\omega_{\text{cell}} = N\epsilon P_{\text{damp}}^2 \tag{1e}$$

where the degrees of freedom $N_f = 3N$, N is the number of particles, and $\mathbf{r}_i$ and $\mathbf{p}_i$ are the position and momentum vectors of the i^{th} particle. A "cell" subscript refers to the simulation cell mass and momentum. The simulation cell "momentum" is modularly invariant, and has $\frac{md^2}{\tau}$ units. $\mathbf{I}$ is the identity matrix, V is the simulation cell volume, $\mathbf{P_a}$ is the applied pressure tensor and $\mathbf{P}_{\text{int}}$ is the internal pressure tensor. The simulation cell "mass" ω_{cell} has units of md^2. Fluctuations in $\mathbf{P}_{\text{int}}$ as the system approaches P_a are dampened by P_{damp} which has units of τ. The energy scale $\epsilon = 1k_n$. As an athermal system, DEM simulations using this barostat ignore contributions typical to molecular dynamics simulations, such as thermostat chains[1] (Shinoda *et al.*, 2004).

The triclinic deformations are captured by the simulation cell matrix $\mathbf{h}$. The $\mathbf{h\Sigma h^T}$ term comes from the Parrinello-Rahman formulation (Parrinello and Rahman, 1981) and represents the external applied stress, defined by reference matrix $\mathbf{h}_0$, where $\Sigma = \mathbf{h}_0^{-1}\left(\mathbf{P}_{\text{int}} - \mathbf{P_a}\right)\mathbf{h}_0^{T-1}$. The internal pressure tensor $\mathbf{P}_{\text{int}}$ components

$$P_{\text{int}}^{\alpha,\beta} = \frac{1}{V}\left[\sum_{i=1}^{N}\frac{\mathbf{p}_i^{\alpha}\mathbf{p}_i^{\beta}}{m} + \mathbf{F}_i^{\alpha}\mathbf{r}_i^{\beta}\right]. \tag{2}$$

At jamming $\mathbf{P}_{\text{int}} = \mathbf{P_a}$ within numerical precision. The left-hand term in Equation 2 is the kinetic energy contribution to pressure P^{kinetic}. A computational, unitless drag factor k_{drag} scales the simulation cell acceleration:

$$k_{\text{drag}} = \quad 1 - \frac{\Delta t f_{\text{drag}}}{P_{\text{damp}}} \tag{3}$$

[1]To exclude thermostat chain and options in LAMMPS (Thompson *et al.*, 2022), add `pchain 0 ptemp 1` to the `fix nph/sphere` barostat options.

where Δt is the time step and f_{drag} is a nonnegative, unitless input parameter[2]. The simulation cell drag factor can mimic experimental packing protocols, or ensure stability flow simulations.

2.2 Packing methodology

For each applied pressure, protocol and friction simulated, 6 packings of $N = 10^4$ monodisperse particles are generated. Property uncertainties are calculated as the standard deviation from the 6 different packings. Simulations are initialized with particles at random positions and low volume fraction $\phi_0 = 0.05$. The initial volume fraction ϕ_0 did not affect the properties of the final packing studied here, so long as ϕ_0 is well below the jamming volume fraction ($\phi_0 < \phi_{\text{jam}} - 0.3$). Initial translational and rotational velocities were set to zero, except when otherwise noted in which case velocities sample a Gaussian distribution with a mean of 0 and a standard deviation to produce an applied initial kinetic energy. The simulation time step was set to $\Delta t = 0.02\tau$. A time step $\Delta t = 0.002\tau$ was also tested and did not change the results for the pressures studied within the uncertainties. After initialization, the particles are isotropically compressed. Although the precise initial state of the particles did not impact the packings, the path to final state has a large impact. Protocol dependence is expected for granular particles, because the system is dissipative and far-from-equilibrium. To sample the possible pathways to pack with a stress-tensor control, particles are compressed using one of the following five Methods:- Method I: slow compression from a dilute state; Method II: slow expansion from a dense state; Method III: repetitive compressions and expansions; Method IV: pressure-controlled progressive de-compression from a dense state; and Method V: volume-controlled progressive de-compression from a dense state. The initial dilute state for all methods was $\phi_0 = 0.05$. Method I applies a constant pressure $P_{a,f}$ at $t = 0$ until the system jams. In Method II, first the system jams at an initial pressure $P_{a,0}$, then the applied pressure is instantaneously changed to $P_{a,f}$. Method III repeats Method II N_{cycle} times, where the system jams after each $P_{a,0}$ and $P_{a,f}$ is applied. The applied pressure is step-wise decreased in Method IV after the system jams at an initial, high pressure $P_{a,0} > P_{a,f}$, by a fraction of $P_{a,0} - P_{a,f}$, re-jamming at each step until the system reaches $P_{a,f}$. Method V is the same as Method IV but volume changes, not pressure, similar to a method used in previous simulations (Silbert, 2010). Protocols I-IV are schematically shown in Figure 1.

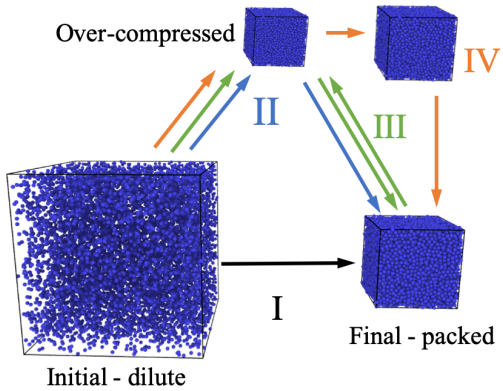

Figure 1: Schematic of the pressure-controlled isotropic compression Methods used in simulations. Procedures are illustrated as arrows for Methods I (black), II (blue), III (green) and IV (orange), and are described in the text.

Beyond the effect of packing protocol and method, the stress tensor can be constrained in different ways. Triaxial compression tests are a close experimental equivalent to the simulation constraints on the stress tensor for isotropic compression (Reddy *et al.*, 1992). However the presented simulations use periodic boundary conditions

[2]Add `drag` f_{drag} to the `fix nph/sphere` options to apply drag on the barostat in LAMMPS (Thompson *et al.*, 2022).

instead of walls. We simulate three cases of applied symmetric stress tensors σ_a: (i) $P_a = \sigma_{a,xx} = \sigma_{a,yy} = \sigma_{a,zz}$ and $\sigma_{a,xy} = \sigma_{a,xz} = \sigma_{a,yz} = 0$, (ii) $P_a = (\sigma_{a,xx} + \sigma_{a,yy} + \sigma_{a,zz})/3$ and $\sigma_{a,xy} = \sigma_{a,xz} = \sigma_{a,yz} = 0$ and (iii) $P_a = \sigma_{a,xx} = \sigma_{a,yy} = \sigma_{a,zz}$, while $\sigma_{a,xy}, \sigma_{a,xz}$ and $\sigma_{a,yz}$ are unspecified and the cell remains rectilinear[3]. At packing in all these simulations, the final stress tensor equals the applied stress tensor. The differences in the stress tensor of the final packings illustrates the importance of understanding the choice of applied stress tensor.

All of the stress-tensor constraints form mechanically stable, jammed configuration. However, the final stress tensors differ. Figure 2a-b shows the six components of the diagonal and off-diagonal components of the stress tensor, respectively, using Method I. The off-diagonal stress components show the largest differences, see Figure 2b. Simulation cells that are not allowed to tilt, where $\sigma_{a,xy}, \sigma_{a,xz}, \sigma_{a,yz}$ are unspecified, had nonzero, albeit small, values of off-diagonal stress at jamming. Those non-zero shear stresses could lead to different yield stresses (Dagois-Bohy *et al.*, 2012). Simulation cells that are allowed to tilt, have off-diagonal stress values that decay to zero, and average angles off the orthorombic box of $90 \pm 0.003°$, for all frictions and pressures tested. The diagonal components of stress $\sigma_{a,xx}$, $\sigma_{a,yy}$ and $\sigma_{a,zz}$ are less affected by the constraints. Unless noted otherwise, simulations in Sec. 3 set diagonal members of the applied stress tensor to the pressure, $P_a = \sigma_{a,xx} = \sigma_{a,yy} = \sigma_{a,zz}$, and off-diagonal members to zero, $\sigma_{a,xy} = \sigma_{a,xz} = \sigma_{a,yz} = 0$. Such precise control on stress is usually unattainable for experimental packing schemes. However the differences in final states demonstrate the importance of knowing the relevant stress and volume controls in experimental and simulation protocols.

Using Method I and the stress constraint defined as case (i), a representative simulation time progression of the kinetic energy, volume fraction and pressure are shown in Figure 2c. At $t = 0$ the kinetic energy and pressure are zero, except for cases with defined initial pressure discussed in Sec. 3.2, at the initial volume fraction $\phi = 0.05$. As the simulation cell volume decreases and picks up momentum, the particle velocities increase due to affine motion, and the kinetic energy and pressure increase. At $t \simeq P_{\text{damp}}$ the Parinello-Rahman algorithm starts to control the pressure and the simulation cell momentum, and the kinetic energy decreases. Near jamming, the kinetic energy decreases by several orders of magnitude and the volume fraction plateaus. The pressure jumps to the applied value as contacts form, with the full applied stress tensor satisfied by the constraints. The near-jamming behavior was similar for all systems studied. However, there are differences at earlier time based on the barostat parameters and initial configuration. Lower values of drag approach the applied pressure faster but with more oscillations.

The volume fraction ϕ and coordination number Z are the key parameters calculated in this study. Both ϕ and Z are calculated without "rattlers", particles that have too few contacts to contribute to the mechanical stability of the packings. Rattlers are identified if $Z_i < 4$ for frictional particles ($\mu_s > 0.01$) and $Z_i < 6$ for frictionless particles, where Z_i is the number of contacts of particle i. The critical friction value $\mu_s = 0.01$ was chosen because it is the point where friction has an appreciable impact on ϕ and Z (Santos *et al.*, 2020). Rattlers are identified iteratively, so that the number of contacts per particle decreases based on the number of rattlers in contact with the particle. If the number of contacts decrease enough to constitute a rattler, by removing neighboring rattlers, it is counted as such. The fraction of rattlers ranges from 0.1% to 10%, correlates with the Z, and depends on μ_s and P.

All of the packings generated were taken from the final simulation configuration, after the simulation was run for at least twice the jamming time. The time to jam depends on the method, the particle and barostat parameters, and therefore some simulations ran longer than others. The inflection point of the kinetic energy, plotted as symbols in Figure 2c, corresponds well with the point where volume fraction stops changing and is a good estimate of the time to jam. However, the volume fraction is not strictly constant once the simulation cell stops moving, and increases slowly for some longer time. To allow for these changes, we run to $t/\tau = 10^6$ for $P_a = 10^{-4}$, $f_{\text{drag}} = 0.0$ and $P_{\text{damp}} = 2.25$ which is well above the time to jam $t_{jam} \sim 1.5\text{x}10^4\tau$. The inflection point in kinetic energy defines t_{jam} (see Fig. 2). The time to jam is inversely proportional to the applied pressure,

[3]To apply those symmetric stress tensors in LAMMPS (Thompson *et al.*, 2022), use `fix nph/sphere` with the following options: (i) `xy 0 0 1 xz 0 0 1 yz 0 0 1` and (ii) `xy 0 0 1 xz 0 0 1 yz 0 0 1 couple xyz`. Case (iii) does not need additional options. See LAMMPS documentation for more details.

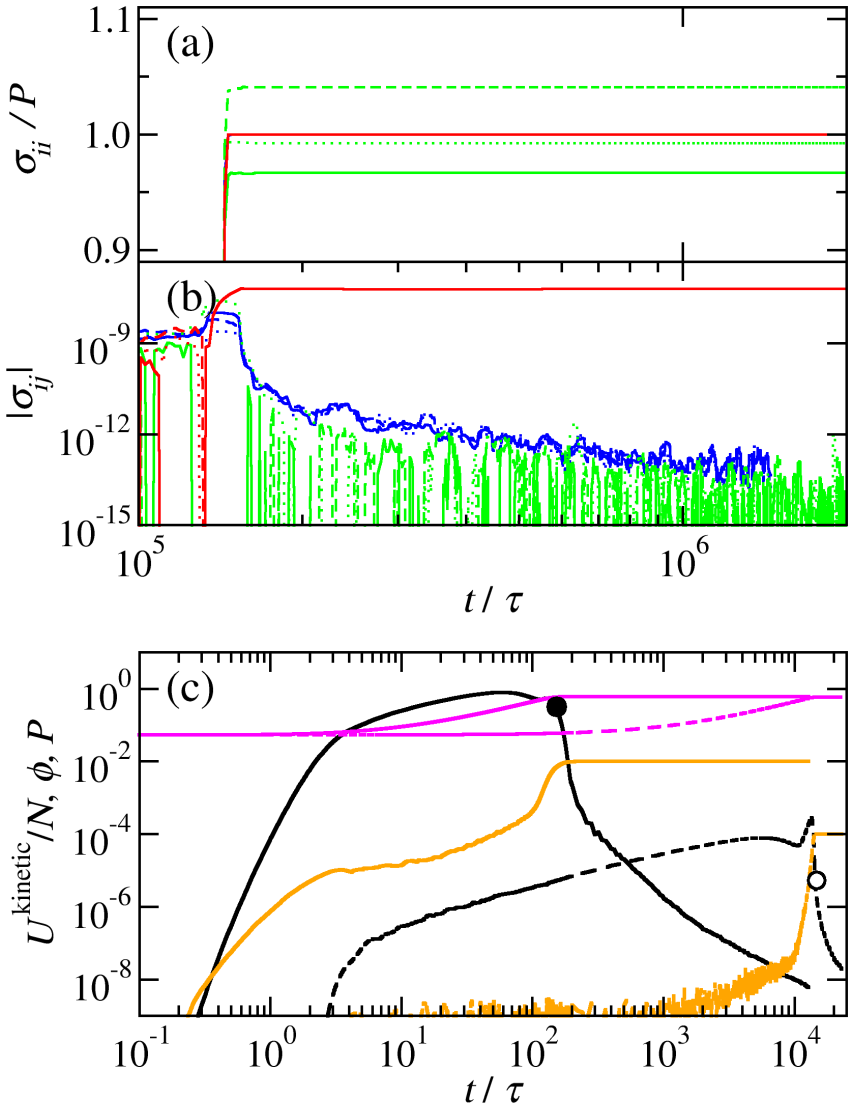

Figure 2: The (a) diagonal and (b) off-diagonal components of the measured stress tensor for $P_a = 10^{-5}$. Three applied stress tensor constraints are plotted: $P_a = \sigma_{a,xx} = \sigma_{a,yy} = \sigma_{a,zz}$, $\sigma_{a,xy} = \sigma_{a,xz} = \sigma_{a,yz} = 0$ (blue), $P_a = (\sigma_{a,xx} + \sigma_{a,yy} + \sigma_{a,zz})/3$, $\sigma_{a,xy} = \sigma_{a,xz} = \sigma_{a,yz} = 0$ (green) and $P_a = \sigma_{a,xx} = \sigma_{a,yy} = \sigma_{a,zz}$, with unspecified values of $\sigma_{a,xy}, \sigma_{a,xz}$ and $\sigma_{a,yz}$ (red) using packing Method I. The different components of the stress tensor are plotted as different line types: xx, xy (solid), yy, xz (dashed) and zz, yz (dotted). The off-diagonal components of the stress tensor are shown as averages over 10 timesteps for clarity. The red lines lie on top of the blue lines because they have the same diagonal applied stress components in (a). (c) The kinetic energy (black), measured pressure (orange) and the volume fraction (magenta) as a function of time for $P_a = 10^{-2}$ (solid lines) and $P_a = 10^{-4}$ (dashed lines) using Method I. The applied stress tensor is: $P_a = \sigma_{a,xx} = \sigma_{a,yy} = \sigma_{a,zz}$, $\sigma_{a,xy} = \sigma_{a,xz} = \sigma_{a,yz} = 0$. The jamming time $t_{\rm jam}$, determined as the inflection point of the kinetic energy for $t > P_{\rm damp}$, is plotted as black circles for $P_a = 10^{-2}$ (filled) and $P_a = 10^{-4}$ (open). For (a), (b) and (c) the simulation cell parameters are $P_{\rm damp} = 2$ and $f_{\rm drag} = 0.1$, and the friction state is $\mu_s = 0.2$.

$t_{\rm jam} \propto \frac{f_{\rm drag}}{P_a P_{\rm damp}}$, and thus the simulation time was scaled accordingly for lower P and/or higher $f_{\rm drag}$.

3 Results

3.1 Packing method dependence

To explore different routes for frictional particle packing (Silbert *et al.*, 2002; Shundyak *et al.*, 2007; Silbert, 2010), we applied various isotropic compression methods to particles with sliding friction. In this subsection the packings were formed at different applied pressures P_a, where the internal pressure of the mechanically stable packing $P_{\rm int} = P_a$, with sliding friction $\mu_s = 0.2$. The packing volume fraction is between the frictionless and high friction limits at $\mu_s = 0.2$, where $\mu_s = 0.2$ is in the middle of experimentally observed material friction range (Farrell *et al.*, 2010). The low-pressure range can be jammed stably, at low computational cost. The packing behavior generated by pressure-controlled compression Methods I-V are shown in Figure 3 and detailed in Sec. 2.2.

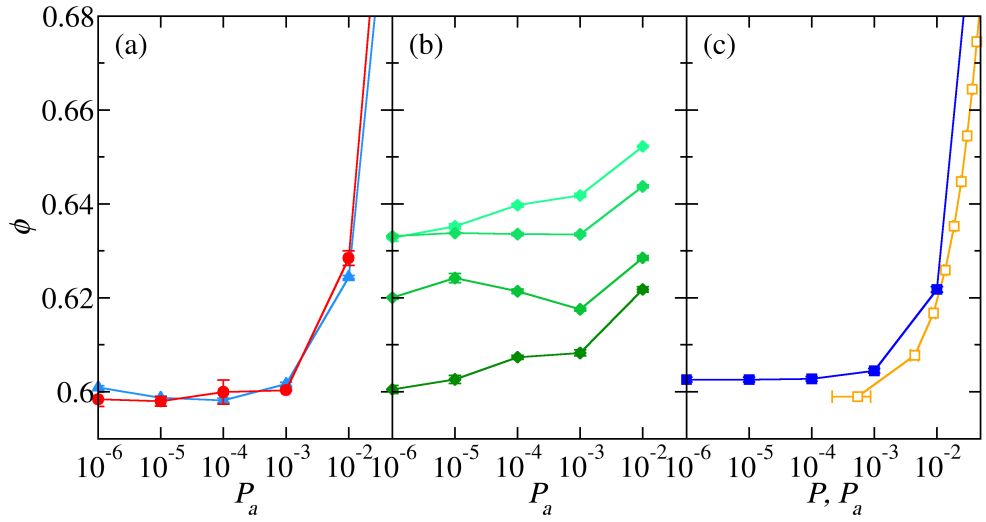

Figure 3: (a) Method I (red circles) packing fraction as a function of pressure $\phi(P_a)$ is compared with Method II (light blue triangles), where $P_{a,0} = 10^{-4}$ and $P_{a,f} = P_a$. (b) Method III, akin to tapping, is shown after different number of compressions $N_{\rm compress} = 1$ (dark green diamonds), 10, 100 and 1000 (light green diamonds). The packings are compressed to $P_{a,0} = 10^{-1}$ in between relaxations. (c) Progressive compression Methods with stress- (IV, blue squares) and volume- (V, orange squares) control show different ranges of pressure. The initial large stress for Method IV t is $P_{a,0} = 10^{-1}$. Method V volume step changes were constant $\Delta\phi = 0.01$. Particles are frictional $\mu_s = 0.2$, and are packed with simulation cell parameters $P_{\rm damp} = 2.25$ and $f_{\rm drag} = 0$. Uncertainties are similar to the symbol size.

Figure 3(a) shows Methods I and II, under- and over-comperssion. Method I applies a pressure at $t = 0$ to a dilute packing; a lower pressure translates to slower compression. Method II follows Method I at first, where a initial pressure is applied $P_{a,0}$ to a dilute system ($\phi = 0.05$) to form a mechanically stable packing. A lower pressure $P_{a,f}$ is applied to the packing formed at $P_{a,0}$ to form a new mechanically stable packing. The pressure on the x-axis of the left panel of Figure 3 is the $P_{a,f}$ for Method II. The Supplementary Information includes Method II packing fractions with other initial pressures $P_{a,0}$. As expected (O'Hern *et al.*, 2003; Silbert, 2010), ϕ from Method I, decreases monotonically. Although the absolute values between Methods I and II are similar, Method II has a minimum with pressure. The non-monotonic pressure dependence is analyzed in Sec. 3.2.

Like Method II, Method III can lead to monotonic or non-monotonic $\phi(P_a)$. Method III, essentially, cyclically repeats method II. The first cycle in Method III, $N_{\rm cycle} = 1$, is the same as Method II with the $P_{a,0} = 10^{-1}$, at which point there is no minimum in $\phi(P_a)$, shown in Figure 3b. The minimum in $\phi(P_a)$ appears after a few cycles ($5 < N_{\rm cycle} < 100$) and disappears at higher cycles ($N_{\rm cycle} > 100$).

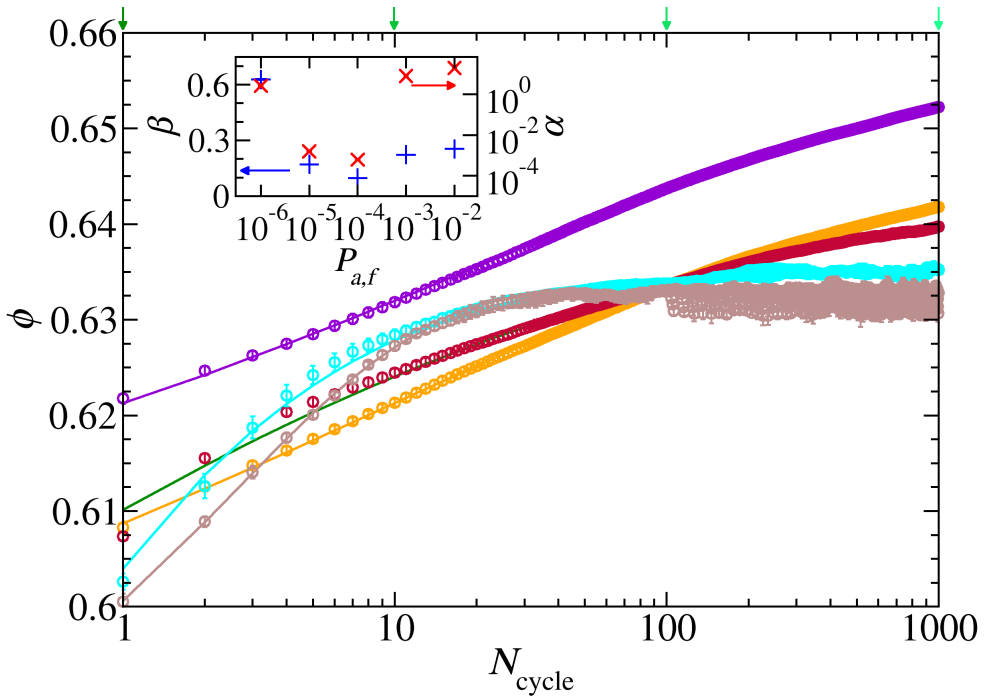

Figure 4: Volume fraction ϕ increases monotonically with N_{cycle} using Method III, by cycling from $P_{a,0} = 10^{-1}$ to different low-pressure compression values $P_{a,f} = 10^{-2}$ (magenta), 10^{-3} (orange), 10^{-4} (dark red), 10^{-5} (cyan) and 10^{-6} (brown). Lines drawn are stretched-exponential fits to simulation data (see Eq. 4). The KWW fit parameters α (red crosses, right inset axis) and β (blue pluses, left inset axis) are plotted in the inset as a function of the applied pressure P_a. The arrow colors at the top of the graph indicate the number of compressions that correspond with the $\phi(P)$ data shown in Figure 3(b). Uncertainties are similar to the symbol size.

The non-monotonic $\phi(P_a)$ behavior, seen in Figure 3b, occurs over a range of N_{cycle}, shown in Figure 4. For each P_a, $\phi(P_a, N_{\text{cycle}})$ increase monotonically with N_{cycle}. Lower pressures $P_a < 10^{-4}$, compact at a faster rate with respect to N_{cycle} and saturate as $N_{\text{cycle}} \to \infty$. The lower P_a packing fractions crossing the higher P_a values, around $N_{\text{cycle}} = 5$ and $N_{\text{cycle}} = 70$, is the same result as the non-monotonicity observed in $\phi(P_a)$, see Figure 3b. Yet, since the lower P_a packings compaction asymptotes at fewer N_{cycle}, higher P_a packings are denser, and $\phi(P_a)$ is monotonic at higher N_{cycle}. The lower pressures have a larger difference with $P_{a,0}$, which allows more time to pack and re-form contacts to build more compact networks with fewer N_{cycle}. At high N_{cycle} Method III forms denser packings with more predictable monotonic $\phi(P_a)$ behavior.

The behavior observed in the $\phi(N_{\text{cycle}})$ are captured by fits to a Kohlrausch-Williams-Watts (KWW) law (Kohlrausch, 1854; Williams and Watts, 1970):

$$\phi(N_{\text{cycle}}) = \phi_\infty - (\phi_\infty - \phi_0)e^{-(N_{\text{cycle}}/\alpha)^\beta} \tag{4}$$

where the fitting parameters are ϕ_∞, ϕ_0, α and β. The intercept ϕ_0 and asymptote ϕ_∞ values are monotonic, inferred by the low and high N_{cycle} curve values in Figure 4. The Figure 4 inset shows that the parameters α and β are nonmonotonic with pressure. The KWW fit parameters α and β quantify the trends in $\phi(N_{\text{cycle}}, P_a)$ and show different behavior above and below $P_a = 10^{-4}$.

The KWW and a logarithmic heuristic (Knight *et al.*, 1995) fits have been applied to experimentally tapped packings. The KWW fit had consistently lower residual standard deviations, compared to logarithmic heuristic fit for the presented data, as seen by (Richard *et al.*, 2005). Method III is considerably different from the experimental tapping protocols (Knight *et al.*, 1995; Philippe and Bideau, 2002), which are compressed in all directions, have no walls and vary the peak tap acceleration, not the pressure, and lead to denser volume fractions $\phi > 0.64$. KWW fits to experimental data (Knight *et al.*, 1995; Philippe and Bideau, 2002) parameters range from $1 < \alpha < 500$ and $0.14 < \beta < 0.65$. Simulation and experimental exponential KWW fit parameter β are in

the same range. The α fit parameters have a different meaning in experiments, which track $\phi(t)$ not $\phi(N_{\text{cycle}})$, in which case α is a rate. However both experiments and simulations found that β increase and α decreases with increasing packing intensity. However the DEM simulations showed that, like experimental tapping, "loose" packings compact with tapping (Knight *et al.*, 1995; Rosato *et al.*, 2010). Kumar and Luding (2016) observed similar behavior and found that memory of the deformation theory could explain the denser-than-experiments volume fractions.

Methods IV and V, shown in Figure 3c, differ from Method II by gradually, instead of instantaneously, decreasing the applied, target pressure, at each step allowing the particles to pack after expansion. Method IV uses pressure-controlled compression, like in Methods I-III, and in Method V the volume is decreased by $\Delta\phi = 0.01$. Smaller volumetric decreases can lead to looser packings (Silbert, 2010). Neither Method IV or V has a minimum in $\phi(P_a)$, as observed in Method II. The absence of a minimum is likely because the volume change is not large enough to break-up the majority of the contact network. Stable packings could not be formed with Method V for $\phi < 0.599$ and $P < 5\text{x}10^{-4}$. Silbert (2010) observed similar volume-controlled packing limits. Ramped-pressure compression simulations of cohesive, frictional grains have exhibited strong history and protocol dependence (Nan and Hoy, 2023). These Methods show that stable packings of the same model frictional particles with the same stress state can have a wide range of volume fractions, and are protocol dependent.

3.2 Non-monotonic volume fraction-pressure dependence

Depending on the packing protocol, the final packing volume fraction can increase with decreasing pressure. The minimum in $\phi(P_a)$ shown in Figure 3a-b for packing Methods II and III showcases the protocol-dependent nature of the packing process. A minimum is not observed in the coordination number, which is relatively insensitive to packing protocol. This leads to the possibility of two packings with the same volume fraction, but different coordination numbers. The initial kinetic energy, drag coefficient and friction are varied to observe the scale protocol parameter impacts on the non-monotonic behavior.

The initial pressure and kinetic energy are important contributions to the packing microstructure. Packings in Figures 3 and 4 were initiated with zero initial kinetic energy and pressure. Increasing the average initial particle translational kinetic energy causes a volume fraction minimum using packing Method I. Figure 5a shows the role of initial kinetic energy contribution to pressur P_i^{kinetic} (see Eq. 2). The $\phi(P_a)$ non-monotonicity is more pronounced with increasing P_i^{kinetic}. Figure 5b demonstrates that packings with the same particle interactions can be made with the same volume fraction, for example $\phi = 0.62$, with an average one fewer contact per particle (compare $P_i^{\text{kinetic}} = 9.5 \times 10^{-2}$ at $P_a = 10^{-6}$ and 10^{-2} in Figure 5). The Figure 5a inset shows that low-pressure volume fraction $P = 10^{-6}$ increases with increasing initial kinetic energy contribution to pressure P_i^{kinetic}, but has a limit of about $\Delta\phi = 0.03$. The Supplementary Information shows the role of initial kinetic energy on the transient approach to packing and on Method II packings.

The minimum value of ϕ in Figure 5a occurs at $P_a = 10^{-4}$, comparable to the lowest pressures (for intermediate to high μ_s) accessible in volume-controlled studies (see Figure 3c and references (Shundyak *et al.*, 2007; Silbert, 2010)). The behavior of the cyclical packings, generated with Method III, also transition at $P_a = 10^{-4}$, specifically the KWW fit parameters α and β in the Figure 4 inset. Experimental and simulation tapping studies observed a minimum in ϕ with the number of cycles (Pugnaloni *et al.*, 2010; Carlevaro and Pugnaloni, 2011).

Particle friction is known to lower packing fraction and coordination number, but also changes the $\phi(P_a)$ minima. Packing fractions in Figures 3-5 are from particles with intermediate friction $\mu_s = 0.2$. The non-monotonicity in $\phi(P_a)$ affects the friction dependence of $\phi(\mu_s)$ as shown in Figure 6. The general form of $\phi(\mu_s)$ is similar to previous studies of packing with sliding friction (Shundyak *et al.*, 2007; Santos *et al.*, 2020), however the initial pressure and drag changes the pressure dependence.

For $P_a < 10^{-3}$, frictionless particles approach the hard-sphere limit and ϕ approaches the $\mu_s = 0$ maximally jammed state. The non-monotonicity with pressure occurs for frictions $\mu_s > 10^{-3}$, where the different pressure

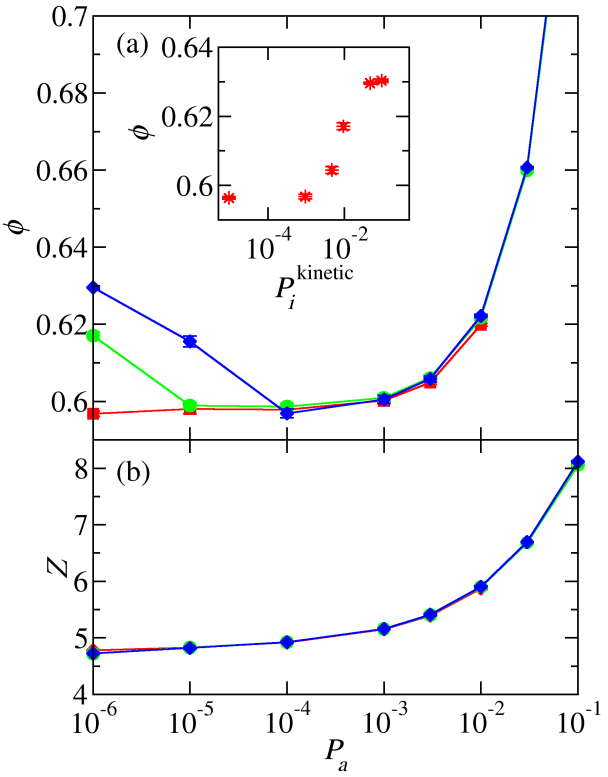

Figure 5: (a) Packing fraction ϕ and (b) average coordination number Z without rattlers as a function of the pressure P_a. Packings were generated with Method I, $P_{\text{damp}} = 2.25$, $f_{\text{drag}} = 0$ and varied amounts of initial total translational kinetic energy contribution to pressure $P_i^{\text{kinetic}} = 0$ (red squares), 9.5×10^{-2} (green circles) and 4.7×10^{-1} (blue diamonds). (inset) Volume fractions as a function of the initial total translational kinetic energy contribution to pressure P_i^{kinetic} at low pressure $P = 10^{-6}$. Coordination number symbols lie on top of each other. Uncertainties are similar to the symbol size.

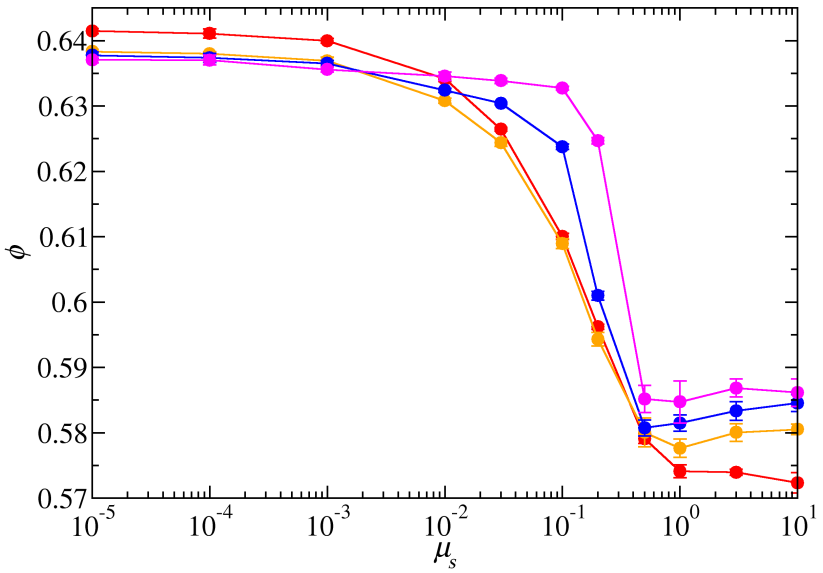

Figure 6: Packing fraction ϕ as a function of sliding friction coefficient μ_s with non-zero initial kinetic energy contribution to pressure $\langle P_i^{\text{kinetic}} \rangle = 9.6 \times 10^{-4}$. Different pressures are shown, $P_a = 10^{-3}$ (red), 10^{-4} (orange), 10^{-5} (blue) and 10^{-6} (magenta). Packings were generated using Method I and protocol parameters $P_{\text{damp}} = 2$, $f_{\text{drag}} = 0.1$.

curves cross. Lowering the pressure narrows the low-to-high μ_s transition, when initialized with non-zero pressure. Although it seems that $\phi(\mu_s)$ tends to a step function as $P_a \to 0$, that behavior depends on protocol. Going to lower pressures to see if a step function arises is computationally difficult because the time to jam the system scales inversely with the applied pressure. The $\phi(\mu_s)$ behavior, as does $\phi(P_a)$, highlights the interdependence of particle interaction and control parameters. Larger pressure, $P_a > 10^{-3}$, behavior of $\phi(\mu_s)$ is shown in the Supplementary Information.

Applying drag in simulations (Delaney *et al.*, 2011; Hoy and Kröger, 2020), or placing particles in density-match fluid in experiments (Farrell *et al.*, 2010), slows the packing and contact formation processes, and forms low-density packings. In simulations, drag, which scales the simulation cell acceleration by $f_{\rm drag}$, also slows the processes. Like the initial kinetic energy contribution to pressure, drag can have significant affect on the final packing fraction. Figure 6 shows data for packings generated with drag, while packings in Figures 3-4 have no drag. Figure 7 shows that although drag can change the volume fraction, a minimum in $\phi(P_a)$ is present for all values of $f_{\rm drag}$ packed using Method I with non-zero initial pressure. For lower pressure, $P_a < 10^{-4}$, the $\phi(P_a)$ minimum is more narrow for larger drag $f_{\rm drag}$. A limiting value of $\phi(P_a \to 0) \simeq 0.63$ is the same with all simulation cell drags. The inset in Figure 7 shows that drag has a small effect on packings when initialized with zero pressure. The $\phi(P_a)$ dependence on $f_{\rm drag}$ demonstrates another of many components of protocol design that impact the final packing of frictional particles.

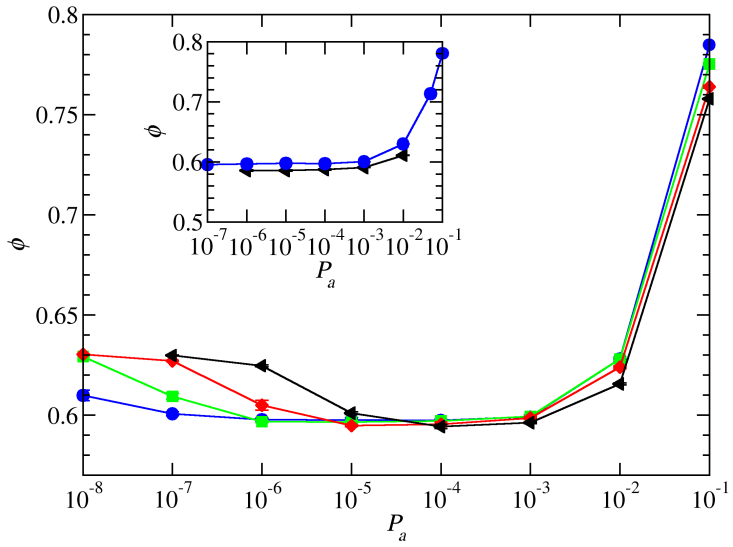

Figure 7: Packing fraction as a function of the pressure $\phi(P_a)$ with particle friction $\mu_s = 0.2$. Initial kinetic energy contribution to pressure $\langle P_i^{\rm kinetic} \rangle = 9.5 \times 10^{-4}$ causes drag-dependent non-monontonic behavior. Drag is applied to the simulation cell by different drag factors $f_{\rm drag} = 0.0$ (blue circles), 0.1 (green squares), 0.3 (red diamonds) and 1.0 (black triangles) with $P_{\rm damp} = 2.25$. (inset) A zero initial kinetic energy contribution to pressure $P_i^{\rm kinetic} = 0$ yields monotonic $\phi(P_a)$ behavior. Packings were generated with Method I. Uncertainties are similar to the symbol size and lines are guides for the eye.

The distribution of contact forces at jamming offers an explanation for the non-monotonicity of volume fraction with pressure. The distributions $F_s/\mu_s F_n$, where F_s and F_n are the magnitudes of the tangential and normal forces respectively, are shown in Figure 8 for the zero and non-zero initial kinetic contribution to pressure cases. As shown in Figure 5, the nonmonotonicity in $\phi(P_a)$ occurs when there is a non-zero initial kinetic contribution to pressure $P_i^{\rm kinetic} > 0$. The probability distribution is normalized so that $\Sigma_{F_s/\mu_s F_n} P(F_s/\mu_s F_n) = 1$. The impact of the $\phi(P_a)$ non-monotonicity is visible in $P(F_s/\mu_s F_n)$ for $P_a \leq 10^{-4}$. For $P_i^{\rm kinetic} = 0$, which does not show non-monotonicity in $\phi(P_a)$, contacts are more likely to be near the Coulomb criterion as the pressure decreases, Figure 8a. For $P_i^{\rm kinetic} > 0$, contacts near the Coulomb criterion ($F_s/\mu_s F_n > 0.94$) become less likely as pressure decreases from $P_a = 10^{-4}$ to $P_a = 10^{-6}$, Figure 8b. $P_i^{\rm kinetic} = 0$ shows the more expected behavior

because $P_a \propto F_n$.

The peak location of $P(F_s/\mu_s F_n)$ is another manifestation of the non-monotonic $\phi(P_a)$ behavior. The peak in $P(F_s/\mu_s F_n)$ is shifted below $F_s/\mu_s F_n = 1$ for $P_a \leq 10^{-4}$ if $P_i^{\text{kinetic}} > 0$. This implies that those larger sliding forces were able to relax due to slower compression. And as the sliding friction contacts weaken, the contacts become less frictional. Seemingly, the tangential constraint sets the average coordination number regardless of its strength. Therefore, the sliding constraint network is maintained as the constraint weakens, but the packing is able to compact. Based on this hypothesis, one would expect the volume fraction to be monotonic not with pressure, but with the number of contacts near the Coulomb criterion. The fraction of contacts near, within 1%, the Coulomb criterion f_{slide}, where $\mu_s F_n = F_s$, also has a non-monotonic dependence with pressure. The $\phi(f_{\text{slide}})$ dependence is shown in Figure 8c. The fraction of contacts within 1% of the Coulomb criterion has an inverse relationship with volume fraction, which yields a monotonic $\phi(f_{\text{slide}})$ relationship, within uncertainty. Based on this discussion the packing microstructure depends on the connectivity of the tangential force network, which sets Z, but the strength of those tangential contacts, specifically the fraction of contacts near the Coulomb criterion, sets ϕ. Similar behavior was observed in other packings and are plotted in the Supplementary Information.

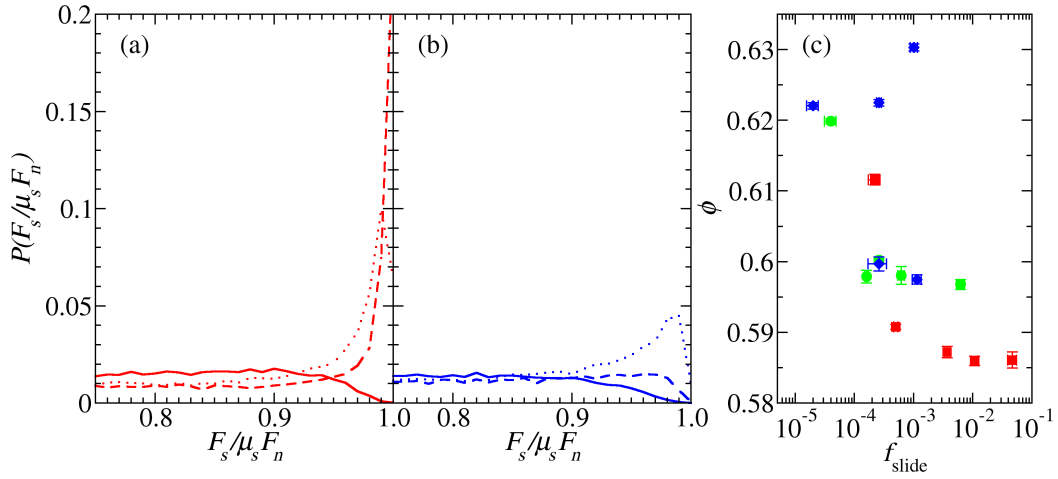

Figure 8: Probability distribution of the tangential force F_s normalized by the maximum, $\mu_s F_n$, for different pressures: $P_a = 10^{-2}$ (solid lines), 10^{-4} (dotted lines) and 10^{-6} (dashed lines). $P_i^{\text{kinetic}} = 0$ (a, red) and $P_i^{\text{kinetic}} > 0$ (b, blue) show different $\phi(P_a)$ behavior. (c) The volume fraction as a function of the fraction of contacts within 1% of the sliding friction Coulomb criterion $\mu_s F_n = F_s$. The packings were generated with Method I and varying amounts of kinetic energy contribution to pressure $P_i^{\text{kinetic}} = 0$ (red squares), 9.5×10^{-2} (green circles) and 4.7×10^{-1} (blue diamonds). Large uncertainties in f_{slide} are due to small absolute denominator values.

4 Conclusion

Simulations of 3-dimensional frictional granular spheres were packed into mechanically stable configurations using pressure-controlled protocols to study the protocol dependence of jamming. The protocols modeled bulk-like packings, with periodic boundary conditions and precisely defining internal states of stress. Five packing protocols were studied including: (I) slow compression from a dilute state, (II) slow expansion from a dense state, (III) repetitive compressions and expansions, (IV) pressure-controlled progressive de-compression from a dense state and (V) volume-controlled progressive de-compression from a dense state.

Non-monotonic packing fraction dependence on pressure was observed in multiple protocols. This led to configurations packed with the same contact mechanics and the same packing fraction, but up to one average contact less per particle. If dilute initial particle configurations were initialized with non-zero velocities or pressure, the packing fraction has a minimum with respect to decreasing pressure. Regardless of the initial kinetic energy, the coordination number decreased monotonicically with pressure. For the cyclical protocol,

Method III, non-monotonic packing fraction pressure dependence occurred for intermediate number of packing cycles. The volume fraction evolution with the number of cycles $\phi(N_{\text{cycles}})$ changed qualitatively with pressure. The parameters for fits to $\phi(N_{\text{cycles}})$ transitioned at intermediate pressure $P = 10^{-4}$. Packings at high pressures compacted continuously with N_{cycles}, but low pressures stopped compacting after $N_{\text{cycles}} = 30$. Future study of the progression of particle correlation and force distribution in these two types of cyclical packings could help model the parameters in the fits to $\phi(N_{\text{cycles}}, P)$.

The tangential force distributions and fraction of frictional contacts were calculated. Low-pressure force distributions were protocol dependent. Low initial kinetic energy, and therefore volume fraction, packings had fewer contacts at and near the Coulomb criteria. The inverse correlation between the volume fraction and the fraction of contacts near the sliding friction Coulomb criterion suggests that lower volume fractions are supported by a higher fraction of frictional contacts. The coordination number and packing fraction are insufficient to define a packing state in this case, frictional particles packed with different protocols. The fraction of frictional contacts is required, as other studies have shown that fabric (Srivastava *et al.*, 2022) and/or stress tensor state (Pugnaloni *et al.*, 2010) may be required. These behaviors disappear for low, but significant enough, frictions $\mu_s < 10^{-2}$, at least in Method I. Packings initiated with non-zero inintial kinetic energy also result in a sharper packing fraction transition with respect to friction coefficient from frictionless to high frictional behavior.

Stress-controlled packing protocol dependence likely reaches beyond properties studied here. Further analysis at the microstructural level, such as properties of the contact network, possibly with the dynamical matrix and fabric tensor, along with a macroscopic approach, such as analysis of the static structure factor and elastic moduli, may further characterize the existence of states with high volume fraction and low coordination number. Particles with more restraints on contacts, those with rolling friction, cohesion or are non-spherical, will also depend on packing protocol, likely in pronounced ways. The protocols presented can be applied to deformation geometries beyond isotropic, such as shear- and extension-jamming. Studies on packing protocol support applying conclusions from well-defined packing protocols to more complex industrial and natural packings.

Conflicts of interest

There are no conflicts to declare.

Acknowledgements

A.S. acknowledges this work was supported, in part, by funding from the NASA Game Changing Development Program. I.S. acknowledges support from the U.S. Department of Energy (DOE), Office of Science, Office of Advanced Scientific Computing Research, Applied Mathematics Program under Contract No. DE-AC02-05CH11231. This work was performed, in part, at the Center for Integrated Nanotechnologies, an Office of Science User Facility operated for the U.S. Department of Energy (DOE) Office of Science. Sandia National Laboratories is a multi-mission laboratory managed and operated by National Technology and Engineering Solutions of Sandia, LLC., a wholly owned subsidiary of Honeywell International, Inc., for the U.S. DOE's National Nuclear Security Administration under contract DE-NA-0003525. The views expressed in the article do not necessarily represent the views of the U.S. DOE or the United States Government.

References

Z. Snow, R. Martukanitz and S. Joshi, *Additive Manufacturing*, 2019, **28**, 78–86.

T. M. Wischeropp, C. Emmelmann, M. Brandt and A. Pateras, *Additive Manufacturing*, 2019, **28**, 176–183.

M. Gerhard and M. Reich, *International Review of Hydrobiology*, 2000, **85**, 123–137.

S. Watanabe, M. Hirabayashi, N. Hirata, Na. Hirata, R. Noguchi, Y. Shimaki, H. Ikeda, E. Tatsumi, M. Yoshikawa, S. Kikuchi, H. Yabuta, T. Nakamura, S. Tachibana, Y. Ishihara, T. Morota, K. Kitazato, N. Sakatani, K. Matsumoto, K. Wada, H. Senshu, C. Honda, T. Michikami, H. Takeuchi, T. Kouyama, R. Honda, S. Kameda, T. Fuse, H. Miyamoto, G. Komatsu, S. Sugita, T. Okada, N. Namiki, M. Arakawa, M. Ishiguro, M. Abe, R. Gaskell, E. Palmer, O. S. Barnouin, P. Michel, A. S. French, J. W. McMahon, D. J. Scheeres, P. A. Abell, Y. Yamamoto, S. Tanaka, K. Shirai, M. Matsuoka, M. Yamada, Y. Yokota, H. Suzuki, K. Yoshioka, Y. Cho, S. Tanaka, N. Nishikawa, T. Sugiyama, H. Kikuchi, R. Hemmi, T. Yamaguchi, N. Ogawa, G. Ono, Y. Mimasu, K. Yoshikawa, T. Takahashi, Y. Takei, A. Fujii, C. Hirose, T. Iwata, M. Hayakawa, S. Hosoda, O. Mori, H. Sawada, T. Shimada, S. Soldini, H. Yano, R. Tsukizaki, M. Ozaki, Y. Iijima, K. Ogawa, M. Fujimoto, T.-M. Ho, A. Moussi, R. Jaumann, J.-P. Bibring, C. Krause, F. Terui, T. Saiki, S. Nakazawa and Y. Tsuda, *Science*, 2019, **364**, 268–272.

N. Weiner, Y. Bhosale, M. Gazzola and H. King, *Journal of Applied Physics*, 2020, **127**, 050902.

R. Buarque de Macedo, E. Andò, S. Joy, G. Viggiani, R. K. Pal, J. Parker and J. E. Andrade, *Proceedings of the National Academy of Sciences*, 2021, **118**, e2102267118.

S. Torquato, T. M. Truskett and P. G. Debenedetti, *Phys. Rev. Lett.*, 2000, **84**, 2064.

C. S. O'Hern, L. E. Silbert, A. J. Liu and S. R. Nagel, *Physical Review E*, 2003, **68**, 1–19.

S. Luding, *Nature Physics*, 2016, **12**, 531–532.

A. P. Santos, D. S. Bolintineanu, G. S. Grest, J. B. Lechman, S. J. Plimpton, I. Srivastava and L. E. Silbert, *Phys. Rev. E*, 2020, **102**, 032903.

P. Chaudhuri, L. Berthier and S. Sastry, *Phys. Rev. Lett.*, 2010, **104**, 165701.

T. Bertrand, R. P. Behringer, B. Chakraborty, C. S. O'Hern and M. D. Shattuck, *Physical Review E*, 2016, **93**, 1–7.

I. Srivastava, L. E. Silbert, J. B. Lechman and G. S. Grest, *Soft Matter*, 2022, **18**, 735–743.

G. Y. Onoda and E. G. Liniger, *Physical Review Letters*, 1990, **64**, 2727–2730.

L. E. Silbert, *Soft Matter*, 2010, **6**, 2918–2924.

C. Song, P. Wang and H. A. Makse, *Nature*, 2008, **453**, 629–632.

L. E. Silbert, D. Ertaş, G. S. Grest, T. C. Halsey and D. Levine, *Physical Review E*, 2002, **65**, 1–6.

K. Shundyak, M. Van Hecke and W. Van Saarloos, *Physical Review E*, 2007, **75**, 010301.

E. Somfai, M. Van Hecke, W. G. Ellenbroek, K. Shundyak and W. Van Saarloos, *Physical Review E*, 2007, **75**, 020301.

D. Bi, J. Zhang, B. Chakraborty and R. P. Behringer, *Nature*, 2011, **480**, 355–358.

E. S. Bililign, J. E. Kollmer and K. E. Daniels, *Physical Review Letters*, 2019, **122**, 38001.

B. D. Lubachevsky and F. H. Stillinger, *Journal of Statistical Physics*, 1990, **60**, 561–583.

C. S. O'Hern, S. A. Langer, A. J. Liu and S. R. Nagel, *Physical Review Letters*, 2002, **88**, 075507.

P. Charbonneau, E. I. Corwin, G. Parisi and F. Zamponi, *Physical Review Letters*, 2012, **109**, 205501.

I. Srivastava, L. E. Silbert, G. S. Grest and J. B. Lechman, *Physical Review Letters*, 2019, **122**, 48003.

R. Kohlrausch, *Pogg. Ann. Phys. Chem.*, 1854, **91**, 179–214.

G. Williams and D. C. Watts, *Trans. Faraday Soc.*, 1970, **66**, 80–85.

J. B. Knight, C. G. Fandrich, C. Ning Lau, H. M. Jaeger and S. R. Nagel, *Physical Review E*, 1995, **51**, 3957–3963.

P. Philippe and D. Bideau, *Euro. Phys. Lett.*, 2002, **60**, 677–683.

P. Richard, M. Nicodemi, R. Delannay, P. Ribière and D. Bideau, *Nature materials*, 2005, **4**, 121–128.

A. D. Rosato, O. Dybenko, D. J. Horntrop, V. Ratnaswamy, L. Kondic and M. Carlo, *Phys. Rev. E*, 2010, **81**, 061301.

N. Kumar and S. Luding, *Granular Matter*, 2016, **18**, 58.

S. Dagois-Bohy, B. P. Tighe, J. Simon, S. Henkes and M. Van Hecke, *Physical Review Letters*, 2012, **109**, 1–5.

K. C. Smith, I. Srivastava, T. S. Fisher and M. Alam, *Physical Review E*, 2014, **89**, 042203.

P. A. Cundall and O. D. L. Strack, *Geotechnique*, 1979, **29**, 47–65.

A. P. Thompson, H. M. Aktulga, R. Berger, D. S. Bolintineanu, W. M. Brown, P. S. Crozier, P. J. in 't Veld, A. Kohlmeyer, S. G. Moore, T. D. Nguyen, R. Shan, M. J. Stevens, J. Tranchida, C. Trott and S. J. Plimpton, *Computer Physics Communications*, 2022, **271**, 108171.

W. Shinoda, M. Shiga and M. Mikami, *Physical Review B*, 2004, **69**, 16–18.

M. Parrinello and A. Rahman, *J. Appl. Phys.*, 1981, **52**, 7182.

G. J. Martyna, D. J. Tobias and M. L. Klein, *J. Chem. Phys.*, 1994, **101**, 4177–4189.

K. R. Reddy, S. K. Saxena and J. S. Budiman, *Geotech. Test. J.*, 1992, **15**, 89–105.

G. R. Farrell, K. M. Martini and N. Menon, *Soft Matter*, 2010, **6**, 2925–2930.

K. Nan and R. S. Hoy, *Phys. Rev. Lett.*, 2023, **130**, 166102.

L. A. Pugnaloni, I. Sánchez, P. A. Gago, J. Damas, I. Zuriguel and D. Maza, *Phys. Rev. E*, 2010, **82**, 050301.

C. M. Carlevaro and L. A. Pugnaloni, *J. Stat. Mech.*, 2011, **2011**, P01007.

G. W. Delaney, J. E. Hilton and P. W. Cleary, *Physical Review E*, 2011, **83**, 051305.

R. S. Hoy and M. Kröger, *Phys. Rev. Lett.*, 2020, **124**, 147801.